

Engineering the Electronic Properties of Two-Dimensional Transition Metal Dichalcogenides by Introducing Mirror Twin Boundaries

Komsa, H.-P.; Krasheninnikov, A. V.;

Originally published:

March 2017

Advanced Electronic Materials (2017), 1600468

DOI: <https://doi.org/10.1002/aelm.201600468>

Perma-Link to Publication Repository of HZDR:

<https://www.hzdr.de/publications/Publ-25387>

Release of the secondary publication
on the basis of the German Copyright Law § 38 Section 4.

Engineering the electronic properties of two-dimensional transition metal dichalcogenides by introducing mirror twin boundaries

Hannu-Pekka Komsa*, Arkady V. Krasheninnikov,

Dr. H.-P. Komsa, Dr. A. V. Krasheninnikov
Department of Applied Physics, Aalto University,
P.O. Box 11100, 00076 Aalto, Finland
E-mail: hannu-pekka.komsa@aalto.fi

Dr. A. V. Krasheninnikov
Helmholtz-Zentrum Dresden-Rossendorf,
Institute of Ion Beam Physics and Materials Research,
01328 Dresden, Germany

National University of Science and Technology MISiS,
4 Leninskiy prospekt, Moscow, 119049, Russian Federation

December 22, 2016

Abstract

Grain boundaries in two-dimensional (2D) materials can have marked influence on the material properties. The effects can be not only detrimental, but also beneficial in transition metal dichalcogenides (TMDs), so that controlling the density and type of the boundaries in these systems should be important for engineering their properties. However, this is often possibly only during the growth stage. Molybdenum and tungsten dichalcogenides feature a particular set of 60° mirror twin boundaries, which are reported

to occur upon merging of the growing flakes, to appear during growth to accommodate for the nonstoichiometry of the sample, or to be produced a posteriori by electron irradiation or thermal annealing. Furthermore, different preparation conditions lead to different atomic structure of the boundary, that consequently exhibit different electronic properties. This has obviously garnered interest for the ability to control grain boundary types and densities. In this progress report, we review the recent experimental and theoretical work related to the characterization of mirror twin boundaries. We provide a consistent set of formation energies for the mirror twin boundaries, which then allows us to draw a coherent picture on the formation mechanisms under different conditions. Finally, we analyze the electronic structure of these boundaries and discuss their potential applications.

Keywords: transition metal dichalcogenides, mirror twin boundaries, density functional theory, transmission electron microscope

1 Introduction

Transition metal dichalcogenides (TMD) are a class of layered materials, that have recently been intensely investigated due to the possibility to isolate from bulk samples or manufacture directly their individual layers, which exhibit unique properties [1, 2] related to their reduced dimensionality. In addition to the prototypical molybdenum disulfide MoS_2 , structurally similar materials can be obtained with other chalcogen and transition metals, leading to a variety of material properties. For example optical characteristics were shown to sensitively depend on the number and relative orientation between the layers, and on the interaction with the substrate.[3, 4, 5] Many two-dimensional (2D) TMDs are semiconductors with reasonably high mobility, thus enabling ultrathin optoelectronic applications.[6, 7] Furthermore, the extremely high surface-to-volume ratio is promising for the catalysis and sensing applications.[8, 9, 10]

Monolayers of TMDs can be prepared in several ways. The most straightforward method is the exfoliation of the bulk material either mechanically via the “scotch-tape” method [11] or via liquid exfoliation.[12] Alternatively, monolayers can be grown on a variety of substrates using, e.g., chemical vapor deposition (CVD) or molecular beam epitaxy (MBE). [8, 13, 14] Starting from the seeds, the growth proceeds to form flakes, which then merge together to form a layer. While in certain cases there are preferred directions,[15] flake orientations are generally random and thus the merging leads to the appearance of grain boundaries with

different angles between the crystal orientations across the boundary. Monolayers exfoliated from the synthetic (or natural) bulk material often have larger grain size, since the synthesis is carried out at high temperature and during longer period of time, thereby allowing the sample to reach thermal equilibrium.

Grain boundaries are expected to modify the material characteristics, such as, e.g., electrical transport, mechanical properties, magnetism, or optical response.[16, 17, 18] Van der Zande et al. found enhanced electron transport parallel to GBs and no marked effect for transport perpendicular to GBs.[14] On the other hand, Ly et al. [19] reported that transport properties change when GBs are present and collected statistics on the transport with regard to GB angle. GB of any angle were found to result in decreased mobility.[19] Enhanced or diminished photoluminescence (PL), depending on the GB type,[14] and enhanced biexciton emission from grain boundary regions [20] have also been reported. On the other hand, it is not clear whether these effect arise from the GB per se, or from other changes in the material parameters close to the GB, such as strain, defect concentrations, Fermi-level position etc. The changes to material properties are not always detrimental. As an interesting application involving GBs, memristor was fabricated using MoS₂, where the memristive behavior was ascribed to GB migration.[21]

Concerning their characterization, grain boundaries are often visible as lines in photoluminescence or Raman images.[14] Alternatively, oxidation can be used to make the grain boundaries easier to distinguish under atomic force microscope, scanning electron microscope, or optical microscope.[22, 23] Furthermore, they can be found by forming a bilayer structure with another layer of the same material, since the PL wave length depends sensitively on the relative orientations of the two layers.[5] These methods provide quick and efficient way to locate GBs and assess their concentration, but offer very little information about the type of GB. GBs can also be found by determining the crystal lattice orientations, and consequently sudden changes in it, by e.g. electron diffraction patterns [13, 14] or second-harmonic generation.[24] These methods can yield the GB angle, but still no information of the atomic structure. High-resolution transmission electron microscopy (TEM) is an indispensable tool for studying local atomic structure of 2D materials, as positions of essentially all the atoms can be distinguished. TEM images of the the grain boundaries at the merged flakes were reported in Refs. [13, 14, 25]. Moreover, the electronic structure of the GBs were studied using scanning tunneling microscopy (STM).[26, 27]

In addition, mirror twin boundaries (MTBs) with particular atomic structure between regions with 60° relative orientation were reported.[28, 29, 30] These were observed either upon flake merging, inside grains to accommodate for the

non-stoichiometry, or produced a posteriori by electron beam or thermal annealing treatments.[28, 30, 31, 32] The latter approach led to formation of triangular domains bounded by MTBs. Due to the trigonal (120° rotational) symmetry of monolayer TMDs, this leads to formation of inversion domains. While the atomic structure of the MTB is highly symmetric and well-established from the TEM images, the situation is complicated by the fact that three different atomic structures for the MTBs have been reported, depending on the preparation conditions. Different MTBs show different electronic structures, with some of them representing fairly ideal one-dimensional metallic system. [33, 30] These are promising for studying one-dimensional electron dynamics, such as charge density waves [34] and Mott-Luttinger liquid. The variety of means to produce these MTBs coupled with the existence of different types of MTBs suggests that unprecedented control over the type and density of MTB grain boundaries, and consequently of their properties, could be achieved.

The works cited above all concentrate on certain types of MTBs, formed under particular conditions in particular TMD materials. Moreover it is frequently difficult to realize the differences in the experimental conditions and what would be the corresponding formation mechanism in each case. In this Progress Report we aim at drawing a coherent picture of mirror twin boundaries in 2D TMDs. We review the current knowledge of the 60° mirror twin boundaries in TMDs including $\text{Mo}(\text{S},\text{Se},\text{Te})_2$ and $\text{W}(\text{S},\text{Se})_2$ materials. On the basis of DFT calculations we elucidate the mechanisms of GB formation, whether it is due to flake merging, accommodation of non-stoichiometry, or a posteriori treatments. The relevant experimental data are taken from the literature. Some of the computational results given here are essentially the same as reported in Refs. [30, 32], but in order to have consistent view with the results for all considered MTBs in all considered TMDs, the missing numbers are calculated and reported on an equal footing.

2 Mirror twin boundaries

We start by reviewing the experimental observations of the mirror twin boundaries. To this date, MTBs with three different atomic structures have been reported in various TMD materials. Representative TEM images of these, together with the corresponding atomic structures, are shown in Figure 1. Note, that the atoms are dark in bright field (BF) images, but bright in annular dark field (ADF) images. We denote these three structures as 4|4P, 4|4E, and 5|5I, following the notation adopted in Ref. [28]. In essence, 4|4P MTB contains 4-fold rings sharing a point

at the chalcogen site, 4|4E MTB also contains 4-fold rings but sharing an edge between them, and 55|8 MTB consists of two 5-fold rings next to an 8-fold ring.

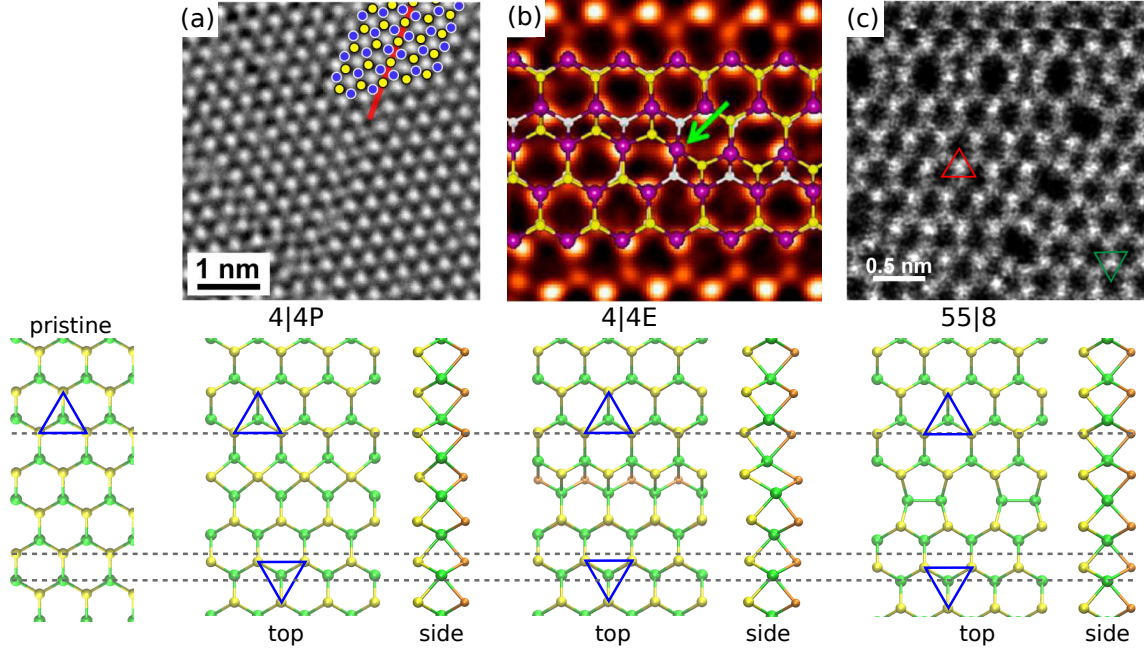


Figure 1: Transmission electron microscopy images for the three MTB structures: (a) 4|4P MTB in MoSe_2 (bright field TEM image), (b) 4|4E MTB in MoS_2 (annular dark field STEM image), and (c) 55|8 MTB in WSe_2 (annular dark field STEM image). Corresponding atomic structures are shown below each panel. The triangles highlight the registry of the lattice at the two sides of the MTB. The dashed horizontal lines highlight strain in the perpendicular direction, when the lattices are aligned at the top. Figures reprinted with permission from: (a) Ref. [30], Copyright 2015 American Chemical Society; (b) Ref. [28], Copyright 2013 American Chemical Society; (c) Ref. [32], Copyright 2015 American Chemical Society.

The 4|4P boundaries tend to be the most commonly observed, at least in the molybdenum chalcogenides. In particular, a large density of these MTBs have been observed to form in MoSe_2 grown by molecular beam epitaxy. [29, 30, 34] This was suggested to originate from the chalcogen deficient stoichiometry of the sample coupled with the low formation energy of MTBs in comparison to the isolated chalcogen vacancies. That is, the chalcogen deficiency is accommodated

by forming MTBs rather than isolated vacancies.[30] This can be compared to the situation in certain non-stoichiometric transition metal oxides, where crystallographic shear planes are found instead of isolated oxygen vacancies.[35] In addition, MoTe_2 grown on MoS_2 substrate also showed a large density of 4|4P MTBs.[36] However, similar observations of large density of these, or any other, MTBs have not been reported in the case of MoS_2 or tungsten chalcogenide growth.

CVD-grown MoS_2 showed, among other smaller angle GBs, 60° grain boundaries of the types 4|4P and 4|4E that were formed upon flake merging.[28] Even for angles deviating from the 60° , the grain boundaries were found to consist of segments of 4|4P MTB with steps exhibiting 8-membered rings.[14, 28, 19] Large triangular inversion domains showing 4|4P MTB, 4|4E MTB, or the mixture of the two types, were observed in MoS_2 following thermal annealing [31]. Their formation was accompanied by creation of vacancies via sulfur desorption.

Several different MTB structures have been formed during electron beam irradiation of different TMD samples at different conditions. Inversion domains consisting of only 4|4P MTBs were observed following electron beam irradiation in MBE-grown MoSe_2 (small grain size) [30] and in CVD-grown MoS_2 (big grain size),[37] both imaged at room temperature (RT). In addition to pure 4|4P ones, inversion domains consisting of a mixture of one 4|4E and two 4|4P MTBs were found in mechanically exfoliated bulk MoSe_2 imaged at RT.[31]

On the other hand, electron beam irradiation led to formation of inversion domains exhibiting only 55|8 MTBs in CVD grown (big grains) MoSe_2 , WS_2 and WSe_2 . [32] Although these experiments were mostly carried out at high temperatures of 500°C , similar structures also appeared at room temperature, albeit at a much slower pace. The same procedure was also applied to MoS_2 , but 55|8 formation could not be achieved.

It is curious that all of these experimentally observed MTBs are rather similar. First and foremost, they all originate from two chalcogen edges. This is a strong indication that they possess very low formation energy versus those formed from metal edges. This was indeed confirmed by first-principles calculations, at least for MoSe_2 , in Ref. [30]. In addition, other MTB configurations, involving chalcogen or metal edges, were considered computationally,[38, 39, 28, 30] but were found to be energetically unfavorable, in line with the lack of the experimental evidence. Second, they also have the same stoichiometry, i.e., they have the same number of the metal and chalcogen atoms in the MTB region. In particular, all of them are chalcogen deficient, which is evident from either calculations of the the number of metal and chalcogen atoms (e.g., within the horizontal dashed lines in

Figure 1, or observations of the local coordination of atoms (either metal atoms are undercoordinated or chalcogen atoms overcoordinated). Thus, their formation entails either addition of metal atoms or removal of chalcogen atoms from the lattice. As shown by the blue triangles in Figure 1, 4|4P structure is laterally shifted by half a lattice constant compared to 4|4E and 55|8 structures.

We note that it is possible to have other types of MTBs, depending on the direction of the GB. For instance, a pure 4|8 structure was observed in the case of 60° GB in armchair direction.[19] By controlling the growth conditions, also triangles featuring Mo-edges or hexagonal shaped flakes with both types of edges can be prepared. Then, upon meeting of two Mo-type edges, MTBs can still form, but obviously with different structures than those discussed here. However, when obtained by annealing or electron beam irradiation, only these three types of MTBs have been observed.

Table 1: Summary of the experimental observations of different MTBs and the assumed origin.

system	4 4P	4 4E	55 8
MoS ₂	grain merge[14, 28, 19], annealing [31], e-beam [37]	grain merge[28], annealing [31]	-
MoSe ₂	growth[29, 30, 34], e-beam[30, 31]	- e-beam [31]	- e-beam [32]
MoTe ₂	growth [36]	-	-
WS ₂	-	-	e-beam [32]
WSe ₂	-	-	e-beam [32]

For the sake of clarity, the experimental observations are collected in Table 1. In the following, we will use first-principles calculations to gain further insight to the stability of the MTBs and also consider the formation kinetics.

2.1 Formation energies of mirror twin boundaries

We start by calculating the interface energies for the MTBs. The energies are expected to give good indication for their relative stability under thermal equilibrium conditions.

In order to allow for relaxation in the direction perpendicular to the MTB, the calculations are carried out in the ribbon geometry. Computational details

are given in Supporting Information.[40] Since all the considered MTBs originate from chalcogen-edges facing each other, the systems contain one unit of MTB and two metal-edges. The relaxed structures are shown in Figure 1, and the actual computational geometry can be seen in Figure 5(c). The lateral size of the supercell is fixed to the lattice constant of each material, but the system is allowed to freely relax in perpendicular direction. The interface energy of the MTB is defined as:

$$E_{\text{MTB}} = E(\text{tot}) - n_{\text{M}}\mu_{\text{MX}_2} - \Delta n\mu_{\text{X}} - 2\gamma \quad (1)$$

where $E(\text{tot})$ is the total energy of the system with MTB, μ_{MX_2} is the energy of pristine MX_2 per formula unit, and Δn is the number of missing chalcogen atoms. The energies of the two Mo/W-edges on both sides of the ribbon are accounted for with the 2γ , which is calculated using triangular flakes.[40] The interface energy also depends on the metal and chalcogen chemical potentials, μ_{M} and μ_{X} , explicitly and through the dependence in γ . We adopt equilibrium with the MX_2 host and metal-rich conditions, yielding $\mu_{\text{M}} = \mu_{\text{M}}^0$ and $\mu_{\text{X}} = \frac{1}{2}(\mu_{\text{MX}_2} - \mu_{\text{M}}^0)$, where μ_{M}^0 is the energy of the elemental phase molybdenum or tungsten.

Table 2: MTB energies E_{MTB} under metal-rich conditions. The two values correspond to calculation where full relaxation in the perpendicular direction is allowed and where the lattice at the edges of the ribbon are fixed (chalcogen sublattice in the case of 4|4P and metal sublattice in the case of 4|4E and 55|8). Energies are in the units of eV.

system	4 4P	4 4E	55 8
MoS ₂	0.38/0.57	0.48/0.68	0.71/0.76
MoSe ₂	0.07/0.20	0.36/0.63	0.41/0.50
MoTe ₂	-0.10/0.02	0.46/0.80	0.25/0.41
WS ₂	0.72/0.95	0.61/0.85	0.82/0.88
WSe ₂	0.35/0.53	0.46/0.80	0.54/0.66

The interface energies for all three MTBs in all of the considered TMDs are listed in Table 2, and can be used to explain the behavior of MTBs during growth [Table 1]. Spontaneous formation of MTBs during growth has only been observed in the case of MoSe₂ and MoTe₂, and showing the 4|4P MTB. While 4|4P is the lowest energy MTB for all materials except WS₂, where 4|4E has the lowest energy, the spontaneous formation additionally requires that the formation energy should be very low. The only systems satisfying this condition according to our calculations are MoSe₂ and MoTe₂, in agreement with the experimental reports.

Upon grain merging, 4|4P and 4|4E have been observed, although there are reports only for MoS₂. In this scenario the meeting flake edges can have arbitrary orientation and spatial shift. While there is no competing structure for the 4|4P-type registry, 4|4E and 55|8 have the same registry and also rather similar “width” of the MTB and thus they are expected to compete energetically. According to our calculations, 4|4E is lower in energy for all materials except MoTe₂, and thus in agreement with observation of only 4|4P and 4|4E MTBs upon grain merging in MoS₂.

In Ref. [31], 4|4E MTB was observed to change into 4|4P in MoSe₂ via shifting of the lattice, which was further enabled by vacancies in the vicinity. This is again in line with 4|4P having lower energy than 4|4E.

According to the above analysis, 55|8 should never be present during growth, except maybe for MoTe₂. Indeed, they were only observed upon electron-beam irradiation. In order to understand their presence in electron beam irradiated samples, the atomic details of the formation mechanism has to be considered in more detail.

3 Mechanism of grain boundary formation under electron beam

The response of TMDs to irradiation by energetic electrons during TEM imaging has already been fairly well understood. Since chalcogens are the outer atoms in the TMD monolayer, and because they are bonded to only 3 neighbors, and often lighter than the metal atoms, the probability for sputtering of chalcogen atoms is higher than for metals. [41, 42, 28, 43, 44] Figure 2(a) shows a number of isolated single S vacancies in MoS₂ near the edge of the monolayer flake. Upon increase of the vacancy concentration, they agglomerate to form vacancy line structures.[45, 31, 37] The agglomeration is enabled by the diffusion of the vacancies, that is further driven by kinetic energy obtained from collisions with the energetic electrons.[45] When concentration of vacancies increases the atomic network becomes unstable with regard to the formation of line defects. An example of the double vacancy line structure in the staggered configuration, which is the lowest energy configuration in many TMDs, is shown in Figure 2(b), and the corresponding atomic structure is illustrated in Figure 2(c). Notice that the structure locally resembles that of 4|4E MTB, although without inverted domains. Only once the chalcogen sublattice is sufficiently depleted, can the metal atoms

get sputtered, which subsequently leads to creation of holes in the sample, or formation of wires or metal atom clusters.[46, 47, 30] Thus, in the following we assume that electron beam can only lead to loss of chalcogen atoms. Thermal annealing should lead to production of S vacancies and thus exhibit a behavior qualitatively similar to electron irradiation.[48, 31]

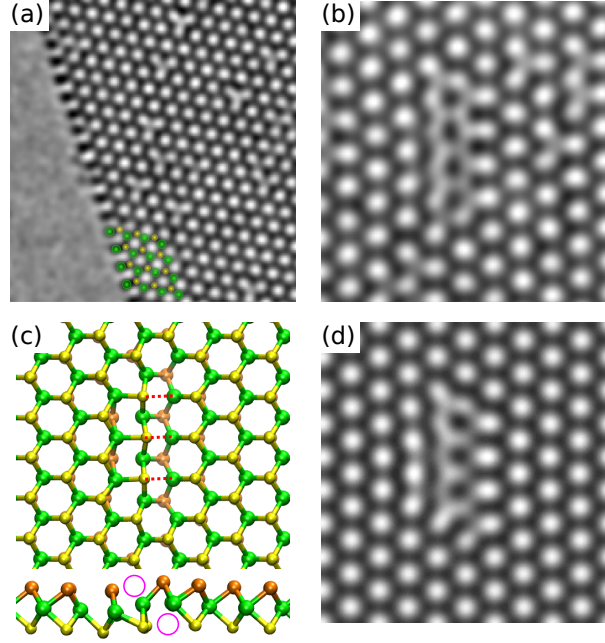


Figure 2: Bright-field TEM images of monolayer MoS_2 showing (a) single S vacancies and (b) staggered double vacancy line. (c) Atomic structure of the the double vacancy line and (d) the corresponding simulated TEM image. Figures reprinted (adapted) with permission from: (a) Ref. [42], Copyright 2012 American Physical Society; (b-d) Ref. [45], Copyright 2013 American Physical Society.

Experimental TEM image sequence for the formation of the inversion domains with all 4|4P MTBs is shown in Figure 3(a-d), with mixed 4|4P and 4|4E MTBs in Figure 3(e-f), and with all 55|8 MTBs in Figure 3(i-k). In the first two cases, the formation is initiated by the appearance of the double vacancy line followed by gliding of the atoms in a triangular domain. In the last case, there are only isolated vacancies and the atomic structure is transformed by a rotation mechanism to be discussed below.

Therefore, in practice, the process will likely proceed once first vacancies are

created by sputtering chalcogen atoms by the electron beam, which gives sufficient freedom for the glides. The exact atomistic kinetic mechanism can be complicated, possess many energetically competitive pathways, and vary between each case. Here, in order to provide an easy to understand overview of the process and related energies, we do not consider the barriers at each step, but only the final configurations. Moreover, to illustrate the structural effects of accommodating inversion areas to pristine lattices, we start from idealized glides of either the metal or chalcogen sublattice within triangular areas, which are then followed by creation of suitable number of vacancies. Such processes with the steps needed to create all three considered MTBs are illustrated in Figure 4.

As shown in Figure 4(a-b), gliding the metal sublattice to the hexagon center positions readily leads to formation of inversion domains with two sides having 4|4P MTBs. The remaining side of the triangle, on the other hand, consists of two S-edges separated by a fairly large distance. When the atomic geometry of this structure is optimized using density-functional theory (DFT), the two sides do not stitch up, since this would lead to large strain and also to MTB with unfavorable atomic configuration. The lattice can be “healed” to full 4|4P domain by further gliding the atoms in the gray shaded area: either gliding only the metal-atoms by one whole lattice vector to the direction of the black arrow or forming double vacancies at the interface and then gliding the whole lattice. If the glide occurs only at one corner, it will lead to dislocation core on the other corner. Healing could also be obtained by adding metal atoms to the vacant sites, but this cannot happen under electron beam irradiation. The registry of the inversion domain and the surrounding lattice is such that formation of 4|4E or 55|8 MTBs at the remaining side leads to rather strong strain. Creating the double vacancies and straightforwardly relaxing the structure without any gliding led to this side of the triangle showing 55|8 MTB. By creating lines of vacancies in staggered configuration, 4|4E MTB could also be obtained.

In the process shown in Figure 3(a-d), the formation of 4|4P MTB under electron beam appears to involve a glide (image with blurred triangular region), but was also accompanied by a dislocation core formed near one of the triangle corners. This is consistent with the presumed mechanism of first forming a staggered vacancy line followed by metal sublattice glide. Finally, dislocation core is formed to relax the strain. This is also credible from the kinetic point-of-view, since vacancy lines are likely needed to allow for the glides to take place initially. This is also very similar to the process suggested for the formation of the 24|4P+4|4E triangle,[31] see Figure 3(e-f).

4|4E and 55|8 MTBs can both form via glide of the chalcogen sublattice. This

readily leaves two sides looking similar to 55|8, prior to pairing of the metal atoms. The remaining side would be very rich in chalcogen atoms. By removing the chalcogen-columns marked by red circles in Figure 4(e), it can also be converted to 55|8 MTB.

On the other hand, 4|4E MTBs can be obtained by the glide of both chalcogen sublattices at the central region and only top or bottom chalcogens at the two edges. Alternatively, the glide of the top or bottom chalcogen atoms in the 55|8 MTBs can turn them into 4|4E type. We note, that if the chalcogen glide takes place only at the top or bottom chalcogen plane within the whole triangle, this leads to formation of the octahedral (1T) polymorph of the TMD material [49, 50] instead of inverted domain.

Finally, in Ref. [32] the kinetic mechanism for the formation of 55|8 triangles was proposed to proceed through bond rotations, or to be more precise, by rotations of structural units, as in 2D silica bilayer.[51] Also, the inversion domain growth was gradual, clearly precluding glides of large triangular domains. The initial steps are illustrated in Fig. 3(l-q). The smallest structure, denoted T_1 , already contains 6 chalcogen vacancies. It can further grow once new vacancies are located near the triangle edges.

In order to explain why different MTBs occur upon different conditions, we consider their stability on the basis of the first-principles calculations.

3.1 Formation energies of inversion domains

To investigate the energetics of inversion domains, such triangular structures were constructed within a 10×10 supercell. The structures are presented in Figure 4(c,f,i). Due to different number of vacancies in these systems, the formation energies are normalized to the number of vacancies:

$$E_{ID} = (E(\text{tot}) - n_M \mu_{MX_2} + \Delta n \mu_X) / \Delta n \quad (2)$$

where $E(\text{tot})$ is the total energy of the system, and Δn is the deviation from stoichiometry, i.e., the number of chalcogen vacancies. Energy of the host per formula unit μ_{MX_2} is calculated using the pristine 10×10 supercell. The normalization by Δn also guarantees that there is no dependence on the chemical potential choice, except up to a constant. Finally, this is also justified in light of the experimental findings: for a given number of vacancies, the system can lower its energy by creating MTBs. In essence, the vacancies are then accommodated into the MTBs.

The results are given in Table 3. In addition to the three larger inversion domains, we also considered isolated single vacancy (SV) and double vacancy (DV),

Table 3: Formation energies per vacancy of various defective structures in all considered TMDs under metal-rich conditions. SV stands for isolated single vacancy, DV for isolated (columnar) double vacancy, Stg. is staggered double vacancy line of length 4, T_1 is the smallest 55|8 inversion domain [shown in Figure 3(n)], and 4|4P, 4|4E, and 55|8 inversion domains (ID) correspond to the structures shown in Figure 4(c,f,i).

system	SV	DV	Stg.	T_1	4 4P ID	4 4E ID	55 8 ID
MoS ₂	1.31	1.28	1.14	1.18	1.31	1.22	1.15
MoSe ₂	1.59	1.42	1.27	1.10	0.73	1.27	0.99
MoTe ₂	1.96	1.56	1.38	0.98	0.15	1.36	0.79
WS ₂	1.54	1.44	1.50	1.37	2.05	1.68	1.40
WSe ₂	1.82	1.57	1.60	1.23	1.25	1.66	1.18

staggered vacancy line of 4x2, small 55|8 triangle [denoted as T_1 , cf. the structure in Figure 3(n)]. The results for SV, DV, staggered DV line and T_1 in MoS₂, MoSe₂, WS₂, and WSe₂ are essentially the same as in Ref. [32]. The difference in absolute values is mainly related to different choices of chalcogen chemical potential. In addition the results are obtained by relaxing the structures using the same PAW setups and numerical parameters as elsewhere in this paper.

The energies should be compared to those of isolated vacancies or the most favorable types of vacancy clusters. While staggered vacancy lines were found to be the preferred vacancy cluster in MoS₂, [45, 37] the situation seems to be different in tungsten chalcogenides where isolated double vacancies are lower in energy. Moreover, in MoS₂ the staggered vacancy line configuration has lower energy than any of the inversion domains. In all other TMDs, the lowest energy is obtained with one of the inversion domain structures. Unlike the data presented in Table 2, the 55|8 is now lower in energy than 4|4E (4|4P is even lower, but the model is constructed by adding metal atoms, which is unrealistic under electron beam). This can be ascribed to the energy contributions from the triangle corners and from the strain differences. In order to give impression of the strain perpendicular to the MTB, one can refer to the dashed horizontal lines in Figure 1. The 4|4P MTB obtained through metal atom sublattice glide should retain the chalcogen sublattice positions, but there is expansion in the lattice perpendicular to the GB. The 4|4E and 55|8 MTBs in contrast should retain the metal sublattice positions. This seems to hold well in the case of 55|8, but the lattice around 4|4E is contracted, indicating that 55|8 is able to minimize the strain in the lat-

tice. We also performed selected calculations for inversion domains with mixed boundaries. Here we simply note that in MoS_2 , $2 \times (4|4\text{P}) + (55|8)$ was lower in energy than $2 \times (4|4\text{P}) + (4|4\text{E})$ (both formed from the structure shown in Figure 4(b) by creating vacancies). Nevertheless, they were both higher in energy than the corresponding number of isolated vacancies.

3.2 Revisiting the experimental results

The three most relevant experimental results are now discussed in light of the above formation energy results. First, the $4|4\text{P}$ inversion domains [Figure 3(a-d)] in MoSe_2 reported in Ref. [30]: The process proceeds by formation of a double vacancy line, followed by Mo glide. The samples had small grains and thus dislocations could be easily formed to relax the strain, eventually leading to inversion domains with all $4|4\text{P}$ MTBs. Second, the mixed $4|4\text{P}$ and $4|4\text{E}$ inversion domains [Figure 3(e-f)] in MoSe_2 reported in Ref. [31]: Formation process should proceed similar to above, but due to the larger grain size dislocation formation is prohibited. The remaining edge retains the $4|4\text{E}$ structure originating from the double vacancy line, even when calculated formation energies would favor $55|8$ MTB. Additional vacancies in the vicinity can assist in releasing the strain. Third, the $55|8$ inversion domains [Figure 3(i-k)] in several TMDs reported in Ref. [32]: At high temperature, due to the increased movement of the atoms, the system can rapidly overcome energy barriers and explore the energy landscape. Due to the large grain size and relatively low number of vacancies, there is no other mechanism for releasing the strain and thus the lowest energy configuration corresponds to $55|8$ MTB. In tungsten chalcogenides isolated double vacancies appear lower in energy than the staggered vacancy line, which also lends support to this process from the kinetics point-of-view. In MoSe_2 , on the other hand, staggered vacancy line formation should be preferred. We presume, that the effect of high temperature is still sufficient to explain the $55|8$ domain formation.

The energy per vacancy drops as the size of the inversion domain increases, and the contribution from the triangle corners vanishes. The role of strain upon increasing inversion domain size, on the other hand, is not straightforward. To this end, energies in the case of fixed lattice constant in the perpendicular directions were also given in Table 2 and reflect the effect of strain on the MTB energies. In MoS_2 and WS_2 , $4|4\text{E}$ MTB is still lower in energy than $55|8$, whereas in selenides and telluride $55|8$ is lower in energy. We expect these results to be indicative of the lowest energy MTB in the case of large inversion domains. This should then explain why inversion domains dominated by $4|4\text{P}$ and $4|4\text{E}$ MTBs were observed

in MoS_2 after thermal annealing.[31] On the basis of our calculations, similar treatment in selenides and tellurides, on the other hand, is expected to yield 5518 domains, in line with the experiments involving irradiation.[32]

4 Electronic structure

In this section we analyze the electronic structure of the MTBs and discuss possible applications of TMD flakes with MTBs. The band structures and densities of states are presented in Figure 5. 414P and 414E MTBs show bands with large dispersion covering almost the whole band gap range. In addition 414P features another band close to conduction band and 414E another band close to valence band. 5518 on the other hand shows strongly localized states with minimal dispersion.

In the case of 414P and 414E MTBs, the metallic band could increase the overall electronic transport along the direction of the boundary. The effect may not be significant unless there are many parallel MTBs. Additionally, scattering from the MTBs will hinder the transport. While 5518 can also have metallic band, depending on the Fermi-level position, the localized nature of the states likely leads to smaller transition probability. In the direction perpendicular to the MTB, the current flow should be limited by transport between the domains, which is hindered by the spin-valley coupling in these materials. That is, although there are states available at same energy and crystal momentum at the two sides of the MTB, these states have opposite spin or valley index.[52] This effect is particularly pronounced when Fermi-level is close to the valence band due to the large spin-orbit splitting of the valence band maximum states. The experiments indeed tend to suggest that all grain boundaries hinder electrical transport in the sample.[14, 19]

Aside from the transport properties, these structures are of interest due to exhibiting fairly ideal one-dimensional metallic system, [33] that can also be easily studied experimentally. Such systems are promising for studying one-dimensional electron dynamics, such as charge density waves and Mott-Luttinger liquid. The charge density wave (CDW) distortion was reported in Ref. [34].

Finally, when more than one layer is considered, the inversion domain formation in only one layer also leads to unusual stacking between the layers. In particular, while bilayer TMDs obtained from the 2H-polymorph possess inversion symmetry, the region with inversion domain in one layer does not. Consequently these regions should show, e.g., distinct nonlinear optical response, piezoelectronic response, valley dichroism, etc., all of which are normally completely or

partially forbidden in the presence of inversion symmetry.

5 Conclusions

In conclusion, we have reviewed the recent experimental and theoretical work related to the characterization and properties of 60° mirror twin boundaries in layered molybdenum and tungsten dichalcogenide materials. We also carried out first-principles calculations and provided a consistent set of formation energies for the three types of boundaries observed in different materials and in different conditions. We considered both idealized boundaries under different strains as well as local inversion domains formed from pristine TMDs via glides of atomic planes followed by introduction of chalcogen vacancies. These allowed us to draw a coherent picture on the formation mechanisms and the dominant boundary structures under different conditions: (i) occurrence upon merging of the growing flakes, (ii) emergence during growth to accommodate for the nonstoichiometry of the sample, and (iii) production a posteriori by electron irradiation or thermal annealing. Using the formation energy results given here and assuming similar formation mechanisms, predictions for other TMD materials can also be made. Finally, we analyzed the electronic structure of these boundaries and discussed their potential applications. Through understanding of the formation mechanisms, control of the type and density of MTB grain boundaries in TMDs can be achieved, thereby paving the way towards engineering the electronic structure of 2D TMDs through controllable introduction of extended defects.

6 Acknowledgments

We thank the Academy of Finland for the support under Project No. 286279, and through its Centres of Excellence Programme (2012-2017) under Project No. 251748 (HPK). We also acknowledge support from the U.S. Army RDECOM via contract No. W911NF-15-1-0606. AVK also acknowledges the financial support of the Ministry of Education and Science of the Russian Federation in the framework of Increase Competitiveness Program of NUST “MISiS” (#K2-2015-033). We also thank CSC–IT Center for Science Ltd. and Aalto Science-IT project for generous grants of computer time.

References

- [1] Q. H. Wang, K. Kalantar-Zadeh, A. Kis, J. N. Coleman, M. S. Strano. *Nature Nanotechnology* **2012**, 7, 11 699.
- [2] M. Chhowalla, H. S. Shin, G. Eda, L.-J. Li, K. P. Loh, H. Zhang. *Nature Chemistry* **2013**, 5, 4 263.
- [3] K. F. Mak, C. Lee, J. Hone, J. Shan, T. F. Heinz. *Phys. Rev. Lett.* **2010**, 105 136805.
- [4] K. F. Mak, K. He, J. Shan, T. F. Heinz. *Nature Nanotechnology* **2012**, 7, 8 494.
- [5] S. Park, M. S. Kim, H. Kim, J. Lee, G. H. Han, J. Jung, J. Kim. *ACS Nano* **2015**, 9, 11 11042.
- [6] B. Radisavljevic, A. Radenovic, J. Brivio, V. Giacometti, A. Kis. *Nature Nanotechnology* **2011**, 6, 3 147.
- [7] O. Lopez-Sanchez, D. Lembke, M. Kayci, A. Radenovic, A. Kis. *Nature Nanotechnology* **2013**, 8, 7 497.
- [8] H. Li, Z. Yin, Q. He, H. Li, X. Huang, G. Lu, D. W. H. Fam, A. I. Y. Tok, Q. Zhang, H. Zhang. *Small* **2012**, 8 63.
- [9] D. Voiry, H. Yamaguchi, J. Li, R. Silva, D. C. B. Alves, T. Fujita, M. Chen, T. Asefa, V. B. Shenoy, G. Eda, M. Chhowalla. *Nature Materials* **2013**, 12, 9 850.
- [10] D. Kong, H. Wang, J. J. Cha, M. Pasta, K. J. Koski, J. Yao, Y. Cui. *Nano Letters* **2013**, 13, 3 1341.
- [11] K. S. Novoselov, D. Jiang, F. Schedin, T. J. Booth, V. V. Khotkevich, S. V. Morozov, A. K. Geim. *Proceedings of the National Academy of Sciences of the United States of America* **2005**, 102, 30 10451.
- [12] J. N. Coleman, M. Lotya, A. O'Neill, S. D. Bergin, P. J. King, U. Khan, K. Young, A. Gaucher, S. De, R. J. Smith, I. V. Shvets, S. K. Arora, G. Stanton, H.-Y. Kim, K. Lee, G. T. Kim, G. S. Duesberg, T. Hallam, J. J. Boland, J. J. Wang, J. F. Donegan, J. C. Grunlan, G. Moriarty, A. Shmeliov, R. J.

- Nicholls, J. M. Perkins, E. M. Grievson, K. Theuwissen, D. W. McComb, P. D. Nellist, V. Nicolosi. *Science* **2011**, *331*, 6017 568.
- [13] S. Najmaei, Z. Liu, W. Zhou, X. Zou, G. Shi, S. Lei, B. I. Yakobson, J.-C. Idrobo, P. M. Ajayan, J. Lou. *Nature Materials* **2013**, *12*, 8 754.
- [14] A. M. van der Zande, P. Y. Huang, D. A. Chenet, T. C. Berkelbach, Y. You, G.-H. Lee, T. F. Heinz, D. R. Reichman, D. A. Muller, J. C. Hone. *Nature Materials* **2013**, *12*, 6 554.
- [15] D. Dumcenco, D. Ovchinnikov, K. Marinov, P. Lazi?, M. Gibertini, N. Marzari, O. L. Sanchez, Y.-C. Kung, D. Krasnozhon, M.-W. Chen, S. Bertolazzi, P. Gillet, A. Fontcuberta i Morral, A. Radenovic, A. Kis. *ACS Nano* **2015**, *9*, 4 4611.
- [16] Z. Zhang, X. Zou, V. H. Crespi, B. I. Yakobson. *ACS Nano* **2013**, *7*, 12 10475.
- [17] K. Q. Dang, D. E. Spearot. *Journal of Applied Physics* **2014**, *116*, 1 013508.
- [18] X. Zou, B. I. Yakobson. *Accounts of Chemical Research* **2015**, *48*, 1 73, PMID: 25514190.
- [19] T. H. Ly, D. J. Perello, J. Zhao, Q. Deng, H. Kim, G. H. Han, S. H. Chae, H. Y. Jeong, Y. H. Lee. *Nat Commun* **2016**, *7* 10426.
- [20] M. S. Kim, S. J. Yun, Y. Lee, C. Seo, G. H. Han, K. K. Kim, Y. H. Lee, J. Kim. *ACS Nano* **2016**, *10*, 2 2399.
- [21] V. K. Sangwan, D. Jariwala, I. S. Kim, K.-S. Chen, T. J. Marks, L. J. Lauhon, M. C. Hersam. *Nature Nanotechnology* **2015**, *10*, 5 403.
- [22] T. H. Ly, M.-H. Chiu, M.-Y. Li, J. Zhao, D. J. Perello, M. O. Cichocka, H. M. Oh, S. H. Chae, H. Y. Jeong, F. Yao, L.-J. Li, Y. H. Lee. *ACS Nano* **2014**, *8*, 11 11401.
- [23] Y. Rong, K. He, M. Pacios, A. W. Robertson, H. Bhaskaran, J. H. Warner. *ACS Nano* **2015**, *9*, 4 3695.
- [24] X. Yin, Z. Ye, D. A. Chenet, Y. Ye, K. O'Brien, J. C. Hone, X. Zhang. *Science* **2014**, *344*, 6183 488.

- [25] A. Azizi, X. Zou, P. Ercius, Z. Zhang, A. L. Elías, N. Perea-López, G. Stone, M. Terrones, B. I. Yakobson, N. Alem. *Nature Communications* **2014**, *5* 4867.
- [26] Y. L. Huang, Y. Chen, W. Zhang, S. Y. Quek, C.-H. Chen, L.-J. Li, W.-T. Hsu, W.-H. Chang, Y. J. Zheng, W. Chen, A. T. S. Wee. *Nature Communications* **2015**, *6* 6298.
- [27] Y. L. Huang, Z. Ding, W. Zhang, Y.-H. Chang, Y. Shi, L.-J. Li, Z. Song, Y. J. Zheng, D. Chi, S. Y. Quek, A. T. S. Wee. *Nano Letters* **2016**, *16*, 6 3682.
- [28] W. Zhou, X. Zou, S. Najmaei, Z. Liu, Y. Shi, J. Kong, J. Lou, P. M. Ajayan, B. I. Yakobson, J.-C. Idrobo. *Nano Letters* **2013**, *13*, 6 2615.
- [29] H. Liu, L. Jiao, F. Yang, Y. Cai, X. e. Wu, W. Ho, C. Gao, J. Jia, N. Wang, H. Fan, W. Yao, M. Xie. *Phys. Rev. Lett.* **2014**, *113* 066105.
- [30] O. Lehtinen, H.-P. Komsa, A. Pulkin, M. B. Whitwick, M.-W. Chen, T. Lehnert, M. J. Mohn, O. V. Yaz yev, A. Kis, U. Kaiser, A. V. Krasheninnikov. *ACS Nano* **2015**, *9*, 3 3274.
- [31] J. Lin, S. T. Pantelides, W. Zhou. *ACS Nano* **2015**, *9*, 5 5189.
- [32] Y.-C. Lin, T. Björkman, H.-P. Komsa, P.-Y. Teng, C.-H. Yeh, F.-S. Huang, K.-H. Lin, J. Jadcak, Y.-S. Huang, P.-W. Chiu, A. V. Krashennnikov, K. Suenaga. *Nature Communications* **2015**, *6* 6736.
- [33] M. Gibertini, N. Marzari. *Nano Letters* **2015**, *15*, 9 6229.
- [34] S. Barja, S. Wickenburg, Z.-F. Liu, Y. Zhang, H. Ryu, M. M. Ugeda, Z. Hus-sain, Z.-X. Shen, S.-K. Mo, E. Wong, M. B. Salmeron, F. Wang, M. F. Crom-mie, D. F. Ogletree, J. B. Neaton, A. Weber-Bargioni. *Nat Phys* **2016**, *12*, 8 751.
- [35] A. Stoneham, P. Durham. *Journal of Physics and Chemistry of Solids* **1973**, *34*, 12 2127 .
- [36] H. C. Diaz, Y. Ma, R. Chaghi, M. Batzill. *Applied Physics Letters* **2016**, *108*, 19 191606.
- [37] S. Wang, G.-D. Lee, S. Lee, E. Yoon, J. H. Warner. *ACS Nano* **2016**, *10*, 5 5419.

- [38] A. N. Enyashin, M. Bar-Sadan, L. Houben, G. Seifert. *The Journal of Physical Chemistry C* **2013**, *117*, 20 10842.
- [39] D. Le, T. S. Rahman. *Journal of Physics: Condensed Matter* **2013**, *25*, 31 312201.
- [40] Supplementary material.
- [41] Z. Liu, K. Suenaga, Z. Wang, Z. Shi, E. Okunishi, S. Iijima. *Nature Comm.* **2011**, *2* 213.
- [42] H.-P. Komsa, J. Kotakoski, S. Kurasch, O. Lehtinen, U. Kaiser, A. V. Krasheninnikov. *Phys. Rev. Lett.* **2012**, *109* 035503.
- [43] J. Hong, Z. Hu, M. Probert, K. Li, D. Lv, X. Yang, L. Gu, N. Mao, Q. Feng, L. Xie, J. Zhang, D. Wu, Z. Zhang, C. Jin, W. Ji, X. Zhang, J. Yuan, Z. Zhang. *Nature Communications* **2015**, *6* 6293.
- [44] E. Sutter, Y. Huang, H.-P. Komsa, M. Ghorbani-Asl, A. Krasheninnikov, P. Sutter. *Nano Letters* **2016**, *16*, 7 4410.
- [45] H.-P. Komsa, S. Kurasch, O. Lehtinen, U. Kaiser, A. V. Krasheninnikov. *Phys. Rev. B* **2013**, *88* 035301.
- [46] X. Liu, T. Xu, X. Wu, Z. Zhang, J. Yu, H. Qiu, J.-H. Hong, C.-H. Jin, J.-X. Li, X.-R. Wang, L.-T. Sun, W. Guo. *Nature Communications* **2013**, *4* 1776.
- [47] J. Lin, O. Cretu, W. Zhou, K. Suenaga, D. Prasai, K. I. Bolotin, N. T. Cuong, M. Otani, S. Okada, A. R. Lupini, J.-C. Idrobo, D. Caudel, A. Burger, N. J. Ghimire, J. Yan, D. G. Mandrus, S. J. Pennycook, S. T. Pantelides. *Nature Nanotechnology* **2014**, *9*, 6 436.
- [48] H. Qiu, T. Xu, Z. Wang, W. Ren, H. Nan, Z. Ni, Q. Chen, S. Yuan, F. Miao, F. Song, G. Long, Y. Shi, L. Sun, J. Wang, X. Wang. *Nature Communications* **2013**, *4* 2642.
- [49] G. Eda, H. Yamaguchi, D. Voiry, T. Fujita, M. Chen. *Nano Letters* **2011**, *11* 5111.
- [50] Y.-C. Lin, D. O. Dumcenco, Y.-S. Huang, K. Suenaga. *Nature Nanotechnology* **2014**, *9*, 5 391.

- [51] T. Björkman, S. Kurasch, O. Lehtinen, J. Kotakoski, O. Yazyev, A. Srivastava, V. Skakalova, J. H. Smet, U. Kaiser, A. V. Krasheninnikov. *Scientific Reports* **2013**, 3 3482.
- [52] A. Pulkin, O. V. Yazyev. *Phys. Rev. B* **2016**, 93 041419.

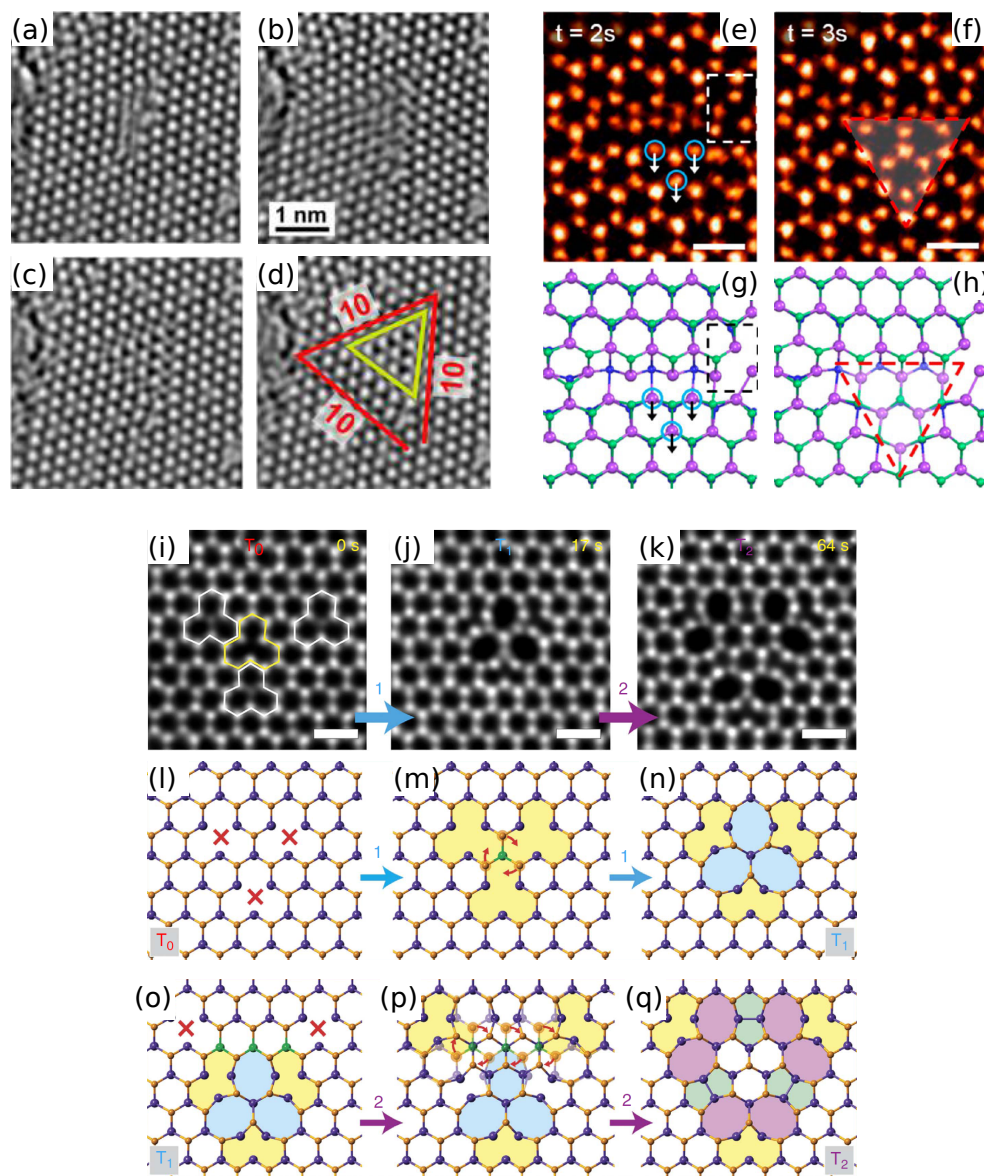


Figure 3: Observations of the inversion domain formation with different mirror twin boundaries. (a-d) BF-TEM image sequence for formation of inversion domain with 4/4P MTBs, starting from double vacancy line followed by a glide. (e-f) ADF-STEM image sequence and (g-h) corresponding atomic structures for a similar process to (a-d), but leading to formation of inversion domain with two 4/4P and one 4/4E MTBs. (i-k) ADF-STEM image sequence for formation of 55/8 inversion domains of increasing size. The atomic mechanisms are illustrated in (l-q). Figures reprinted with permission from: (a-d) Ref. [30], Copyright 2015 American Chemical Society; (e-f) Ref. [31], Copyright 2015 American Chemical Society; (i-q) Ref. [32], Copyright 2015 Nature Publishing Group .

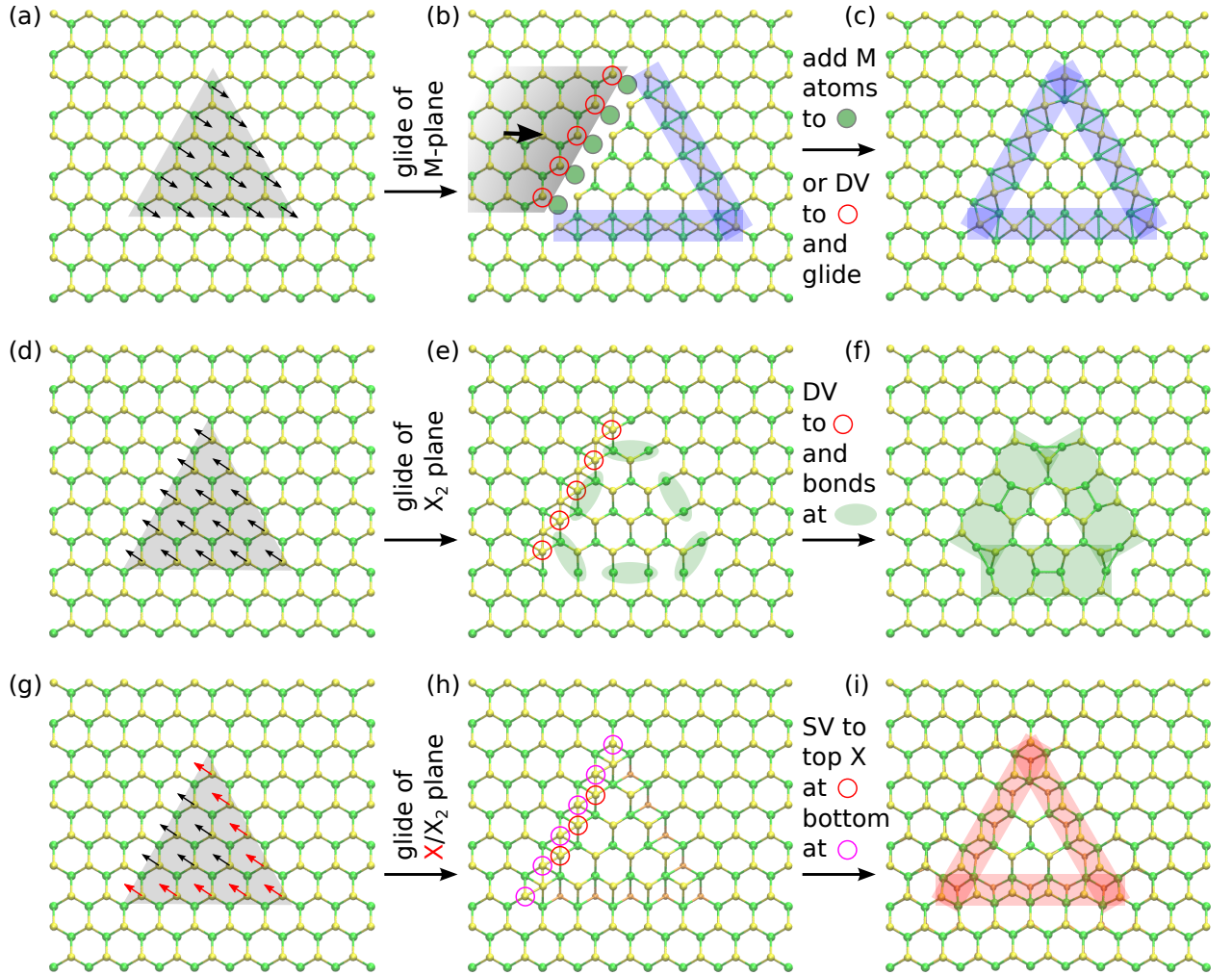


Figure 4: Sketch of the formation mechanisms of the inversion domains with various MTBs via metal or chalcogen sublattice glides. (a-c) 4|4P MTBs through glide of metal sublattice (black arrows), followed by either addition of metal atoms (green circles) or creation of vacancies (red circle) together with additional glide of the lattice (grey shaded area, black arrow). (d-f) 55|8 MTBs through glide of both chalcogen sublattices (black arrows), followed by creation of double vacancies (red circles). Pairing of metal atoms is also illustrated by green ellipses. (g-i) 4|4E MTBs through glide of both chalcogen sublattices (black arrows) or only top or bottom sublattice (red arrow), followed creation of vacancies in the top (red circle) and bottom (magenta circle) sites.

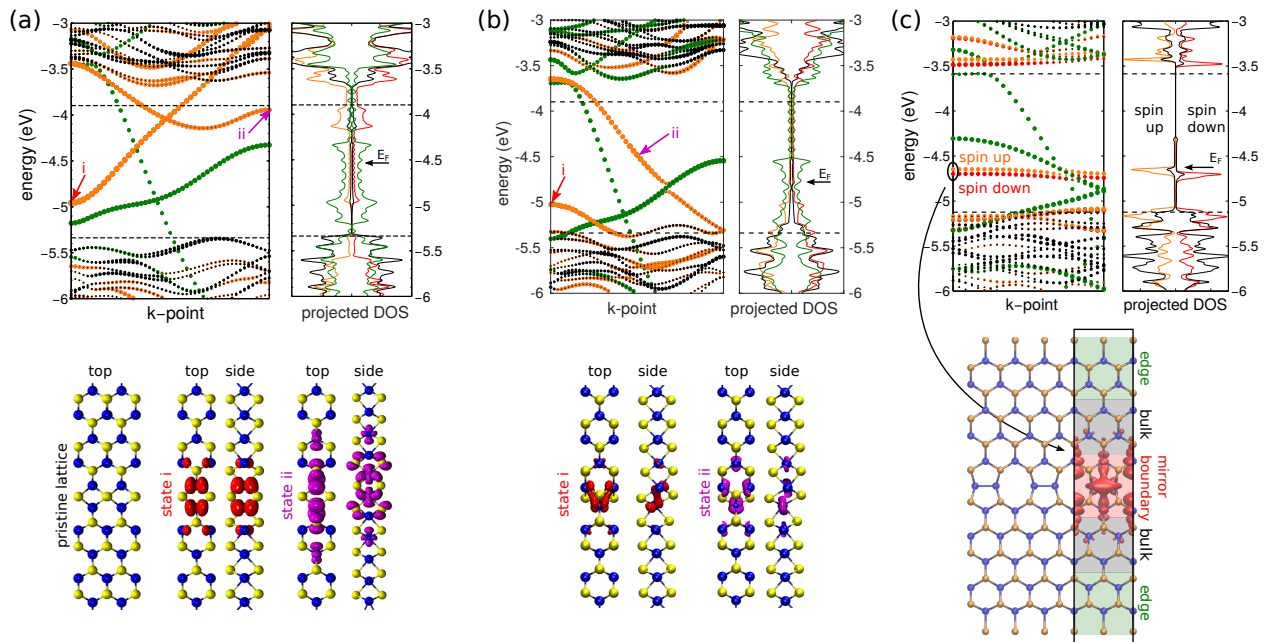


Figure 5: Band structure and density of states for (a) 4I4P MTB, (b) 4I4E MTB, and (c) 55I8 MTB. In all cases, orange (and red), green, and black, denote for states predominantly localized in MTB, ribbon edge, and ribbon interior regions. Partial charge density isosurface for selected MTB-related states are also visualized below. Figures reprinted (adapted) with permission from: (a) Ref. [30], Copyright 2015 American Chemical Society; (c) Ref. [32], Copyright 2015 Nature Publishing Group.